

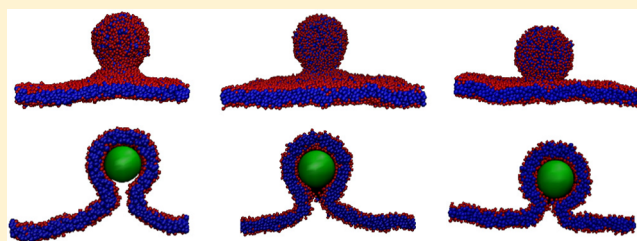
Mechanisms of Budding of Nanoscale Particles through Lipid Bilayers

Teresa Ruiz-Herrero,^{*,†} Enrique Velasco,[†] and Michael F. Hagan^{*,‡}

[†]Departamento de Física Teórica de la Materia Condensada, Universidad Autónoma de Madrid, Madrid

[‡]Department of Physics, Brandeis University, Waltham, Massachusetts 02453, United States

ABSTRACT: We examine the budding of a nanoscale particle through a lipid bilayer using molecular dynamics simulations, free energy calculations, and an elastic theory, with the aim of determining the extent to which equilibrium elasticity theory can describe the factors that control the mechanism and efficiency of budding. The particle is a smooth sphere which experiences attractive interactions to the lipid head groups. Depending on the parameters, we observe four classes of dynamical trajectories: particle adhesion to the membrane, stalled partially wrapped states, budding followed by scission, and membrane rupture. In most regions of parameter space we find that the elastic theory agrees nearly quantitatively with the simulated phase behavior as a function of adhesion strength, membrane bending rigidity, and particle radius. However, at parameter values near the transition between particle adhesion and budding, we observe long-lived partially wrapped states which are not captured by existing elastic theories. These states could constrain the accessible system parameters for those enveloped viruses or drug delivery vehicles which rely on exo- or endocytosis for membrane transport.



INTRODUCTION

The mechanisms by which nanoscale particles cross cell membranes and the factors that control their uptake are essential questions for cellular physiology and modern biomedicine. Regulating the uptake (endocytosis) of nanoparticles is important for nanomedicine applications and for predicting nanoparticle toxicity.^{1–3} Similarly, during the replication of many viruses, an assembled nucleocapsid buds through the cell membrane, simultaneously exiting the cell and acquiring a membrane coating of host origin. Although endocytosis,⁴ viral budding,^{5,6} and scission of budded viruses⁷ can be actively driven or assisted by cell machinery, both nanoparticle uptake and at least some aspects of budding of viruses or viral proteins^{8,9} can occur passively (without cell machinery or ATP hydrolysis).^{10–13} Furthermore, evidence suggests that some viruses do or can undergo passive budding in vivo (e.g., refs 11 and 14). It is therefore important to establish the aspects of particle budding which are generic to passive transport and thus underlie all forms of particle uptake or egress. In this paper we use elastic theory, molecular dynamics (MD) simulations, and free energy calculations to characterize the dynamics and thermodynamics of the process by which a particle adheres to a membrane, is passively wrapped, and then spontaneously separates (Figure 1).

Previous works first studied the equilibrium configurations of budding through a vesicle or infinite membrane as a function of membrane rigidity, particle size, and membrane-particle adhesion energy using elasticity theory.^{15–18} Subsequently, Monte Carlo simulations on a vesicle represented by a randomly triangulated surface¹⁹ and MD on a coarse-grained

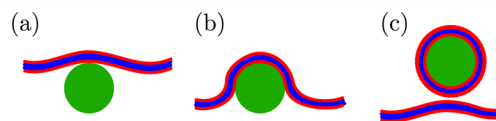


Figure 1. During budding, the particle first adheres to the membrane (a), then is progressively wrapped (b), and finally buds out of the membrane (c).

lipid model²⁰ were used to investigate wrapping of charged particles, while density functional theory was applied to study the relationship between particle hydrophobicity and wrapping.²¹ Dissipative particle dynamics (DPD) was also used to investigate the wrapping of a particle by an inhomogeneous bilayer²² and the wrapping behavior of ligand-coated nanoparticles.²³ Recently, the wrapping behavior of ellipsoidal particles has been studied via DPD²⁴ and MD simulations.²⁵

Although all of these treatments show that the adhesion energy required for wrapping depends on particle properties and membrane composition, there has not been a thorough comparison of predictions of elasticity theory with the results of more sophisticated computational models. In this work our primary objective is to understand the extent to which simplified elastic models can describe the thermodynamics and/or dynamics of particle uptake. To focus on aspects generic to all forms of exo- or endocytosis, we consider a minimal model in which the membrane is treated as a bilayer of

Received: February 17, 2012

Revised: July 16, 2012

Published: July 18, 2012

homogeneous composition and the spherical particle is preassembled, as in the case of nanoparticles or, e.g., type-D retroviruses.^{26,27} Thus, in this work we do not consider the effects of membrane inhomogeneity (i.e., lipid rafts) or the association of viral membrane proteins.^{5,28} We compare the predictions of the elastic model¹⁵ to results of dynamical simulations and free energy calculations. We find that the phase behavior predicted by the two descriptions agrees nearly quantitatively in most regions of parameter space, but there are important dynamical differences at parameter values near the transition between no uptake and particle budding. In particular, we identify a partially wrapped state which we show to be metastable.

METHODS

Membrane Model. We model the amphiphilic lipids comprising the membrane with a coarse grained implicit solvent model from Cooke et al.,²⁹ in which each amphiphile is represented by one head bead and two tail beads that interact via repulsive WCA potentials³⁰

$$V_{\text{rep}}(r) = \begin{cases} 4\epsilon_0 \left[\left(\frac{b}{r} \right)^{12} - \left(\frac{b}{r} \right)^6 + \frac{1}{4} \right] & r \leq r_c \\ 0 & r > r_c \end{cases} \quad (1)$$

with $r_c = 2^{1/6}b$ and b chosen to ensure an effective cylindrical lipid shape: $b_{\text{head-head}} = b_{\text{head-tail}} = 0.95\sigma$ and $b_{\text{tail-tail}} = \sigma$, where σ will turn out to be the typical distance between beads within a model lipid molecule.

The beads belonging to a given lipid are connected through FENE bonds, eq (2),³¹ and the linearity of the molecule is achieved via a harmonic spring with rest length 4σ between the first and the third bead, eq (3)

$$V_{\text{bond}}(r) = -\frac{1}{2}\kappa_{\text{bond}}r_{\infty}^2 \ln[1 - (r/r_{\infty})^2] \quad (2)$$

$$V_{\text{bend}}(r) = \frac{1}{2}\kappa_{\text{bend}}(r - 4\sigma)^2 \quad (3)$$

where $r_{\infty} = 1.5\sigma$.

Since this is an implicit solvent model, the hydrophobicity is represented by an attractive interaction, eq (4), between all tail beads given by

$$V_{\text{attr}}(r) = \begin{cases} -\epsilon_0 & r < r_c \\ -\epsilon_0 \cos^2 \frac{\pi(r - r_c)}{2\omega_c} & r_c \leq r \leq r_c + \omega_c \\ 0 & r > r_c + \omega_c \end{cases} \quad (4)$$

This model allows the formation of bilayers with physical properties such as fluidity, area per molecule and bending rigidity that are easily tuned via ω_c (Figure 2). Moreover, diffusivity within the membrane, density, and bending rigidity are in good agreement with values of these parameters measured for biological membranes.²⁹

Membrane-Particle Interaction. As noted in the Introduction, the systems we have in mind include synthetic nanoparticles or viral particles which bud through attractive interactions with lipid membranes. These interactions can arise in part from electrostatic interactions between charged lipid head groups and charges on the nanoparticle surface or capsid exterior (e.g., basic residues on the matrix protein in

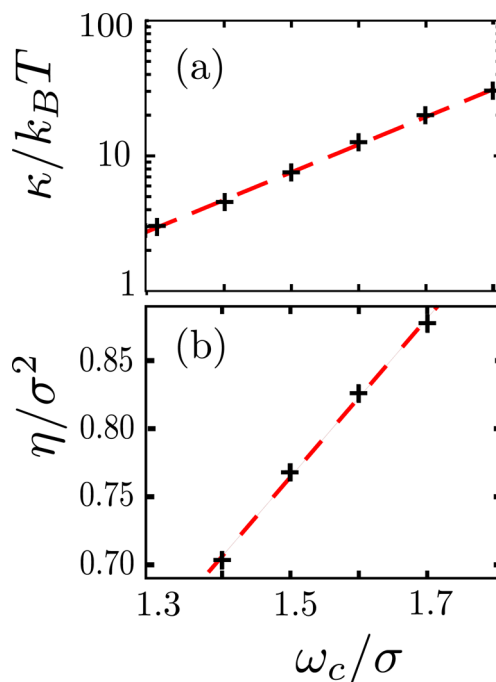


Figure 2. The properties of the membrane are easily tuned by ω_c . (a) Bending rigidity κ (in log scale) and (b) areal density η of lipids as functions of ω_c . The values in (a) are from ref 29, and the values in (b) were calculated from our simulations.

retroviruses⁵). A second source of interaction can be protein mediated, including binding of nanoparticle-functionalized ligands to membrane receptors or insertion of hydrophobic tails on capsid proteins into the membrane.³² Finally, transmembrane viral “spike” proteins can drive or facilitate budding. Importantly, each of these forms of interactions is short ranged. Receptor–ligand and spike protein–virus interactions operate on length scales of Å to nm; similarly, at physiological conditions of 100 mM salt, electrostatic interactions have a Debye screening length of 1 nm. Thus, to keep our analysis general, we consider a short-range attractive interaction between our model particle and head groups. In particular, we represent the combination of excluded volume and attractive interactions between the particle and head groups with a shifted Lennard-Jones potential

$$V_{\text{particle-head}} = \begin{cases} 4\epsilon \left[\left(\frac{\sigma}{r-s} \right)^{12} - \left(\frac{\sigma}{r-s} \right)^6 \right] - V_{\text{cut}} & r < r_{\text{ph}} + s \\ 0 & r \geq r_{\text{ph}} + s \end{cases} \quad (5)$$

with ϵ being a free parameter that controls the membrane-particle interaction strength, $s = R - \sigma/2$, R is the particle radius, $V_{\text{cut}} = 4\epsilon[(\sigma/r_{\text{ph}})^{12} - (\sigma/r_{\text{ph}})^6]$, $r_{\text{ph}} = 3.5\sigma$, and $\epsilon - V_{\text{cut}}$ is the depth of the attractive interaction between the particle and the membrane. Notice that the parameter s shifts the range of the Lennard-Jones interaction so that the membrane interacts with the particle surface instead of with its center.

The particle experiences only excluded volume interactions with the tail groups, which are modeled with a shifted WCA potential³⁰

$$V_{\text{particle-tail}} = 4\epsilon_0 \left[\left(\frac{\sigma}{r-s} \right)^{12} - \left(\frac{\sigma}{r-s} \right)^6 + \frac{1}{4} \right] \quad (6)$$

Adhesion Free Energy. To enable comparison between the simulation results and the elastic theory presented below eq (11), it is important to note that budding is controlled by particle–membrane adhesion free energy rather than simply the depth of the headgroup-particle attractive potential well ϵ . Specifically, the elastic theory will be presented in terms of ϵ^* , the adhesion free energy per area. We calculate this quantity from the simulated potential as

$$\epsilon^*/k_B T = -\eta \log \left[1 + \int_{s+\sigma}^{\infty} dr (e^{-V_{\text{particle-head}}(r)} - 1) \right] \quad (7)$$

The resulting relationship is shown in Figure 3. Here we have neglected the tiny contribution from cutting off the potential,

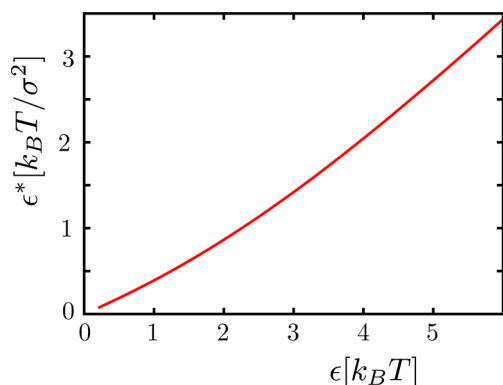


Figure 3. Relationship between the adhesion energy, ϵ , and the adhesion free energy per area, ϵ^* , for $\kappa = 13.9k_B T$.

we assume that each lipid headgroup in contact with the particle approaches roughly along a radial coordinate, and we neglect configurational entropy losses endured by the lipid molecules during adhesion.

Parameters. From the phase diagram in ref.²⁹ we set the temperature of our simulations to $k_B T/\epsilon_0 = 1.1$, which allows for a broad range of ω_c (between 1.3σ and 1.7σ) within which the membrane is in the fluid state. Furthermore, the bending rigidity was calculated as a function of ω_c over this range of values for $k_B T/\epsilon_0 = 1.1$ in the same work; results from that reference are shown in Figure 2a. Values of the bilayer density calculated in our simulations over a similar range of ω_c are shown in Figure 2b.

The units of energy, length, and time in our simulations are respectively ϵ_0 , σ , and τ_0 . The remaining parameters can be assigned physical values by setting the system to room temperature, $T = 300$ K, and noting that the typical width of a lipid bilayer is around 5 nm, and the mass of a typical phospholipid is about 660 g/mol. The units of our system can then be assigned as follows: $\sigma = 0.9$ nm, $m_0 = 220$ g/mol, $\epsilon_0 = 3.77 \times 10^{-21}$ J = 227 gÅ²/ps² mol, and $\tau_0 = \sigma(m_0/\epsilon)^{1/2} = 8.86$ ps.

Simulations. Molecular dynamics (MD) simulations of budding were performed at constant temperature and tension using the velocity Verlet algorithm, with a Langevin thermostat³³ to maintain constant temperature and a modified Andersen barostat³⁴ to simulate a tensionless infinite membrane. This statistical ensemble reproduces the conditions of the cellular environment, where temperature is constant around 37 °C and the membrane is tensionless on average. The time step was $\Delta t = 0.01\tau_0$, the friction constant was $\gamma = \tau_0^{-1}$, the box friction for the Andersen barostat was $\gamma_{\text{box}} = 2 \times 10^{-4}$

and the box mass $Q = 10^{-5}$ in the system units. The reference pressure, P_0 , was set to 0, to simulate a tensionless membrane. The tension equals the pressure because the normal component to the membrane, the z axis in our case, is free to fluctuate and does not contribute to the pressure. The x and y components of velocities and positions were rescaled according to the changes in the volume. In order to simulate an infinite membrane, periodic boundary conditions were employed.

For most simulations the membrane was comprised of $n = 7164$ lipids. An initial bilayer configuration was relaxed by MD and then placed normal to the z axis in a cubic box of side-length $L = 63.5\sigma$. The particle was introduced in the center of the box with its top pole located about 5σ below the membrane surface with zero initial velocity.

Since the membrane was kept tensionless by the barostat, the size of the box decreased during simulations as the particle was wrapped. To ensure that there were no finite size effects, additional sets of simulations were performed, following the same protocol, for membranes with $n = 16\,200$ lipids in an initial box size of $100 \times 100 \times 60 \sigma^3$, and with $n = 28\,800$ lipids in an initial box size of $130 \times 130 \times 60 \sigma^3$. Except where mentioned otherwise, results are shown for the system with $n = 7164$ lipids.

Free Energy Calculations. In addition to performing dynamical simulations of budding, we calculated the potential of mean force as a function of particle penetration using umbrella sampling.³⁵ Simulations were performed in which the system was biased toward particular values of the penetration p by introducing a biasing function $U_{\text{bias}}(\{\mathbf{r}\}) = 1/2\kappa_{\text{umb}}(p(\{\mathbf{r}\}) - p_0)^2$. Here $p(\{\mathbf{r}\})$ is the penetration for a configuration $\{\mathbf{r}\}$ and is defined as the distance between the top of the particle and the center of mass of the membrane. A series of windows were performed at different values of p_0 ; for all windows $\kappa_{\text{umb}} = 200\epsilon_0/\sigma^2$. The simulations were started for an unwrapped particle ($p = -6\sigma$), and initial coordinates for each subsequent window were obtained from simulations in the previous one. Statistics from each window were stitched together and reweighted to obtain the unbiased free energy using the weighted histogram analysis method (WHAM).^{36,37}

An additional set of free energy calculations was performed for $\epsilon = \epsilon_0$ and $R = 12\sigma$ (which lead to metastable partially wrapped states as described below) to improve statistics and to determine if the harmonic potentials were constraining relaxation of other degrees of freedom. A bias potential given by the negative of the already calculated free energy was imposed. Sampling was performed in a series of windows, wherein a smoothed Heaviside function eq (8) constrained the penetration around a window-dependent value of p_0 within a range of 0.4σ

$$U_{\text{Heaviside}} = \begin{cases} \frac{1}{2}\kappa_{\text{umb}}(p(\{\mathbf{r}\}) - p_{\text{max}})^2 & p \geq p_{\text{max}} \\ \frac{1}{2}\kappa_{\text{umb}}(p_{\text{min}} - p(\{\mathbf{r}\}))^2 & p \leq p_{\text{min}} \end{cases} \quad (8)$$

where $p_{\text{max}} = p_0 + 0.2\sigma$ and $p_{\text{min}} = p_0 - 0.2\sigma$

A third set of free energy calculations was performed in which only smoothed Heaviside constraints were applied. Similar unbiased free energies were obtained in each case, indicating that relaxation of other degrees of freedom was satisfactory. Histograms from all sets of free energy calculations were then stitched together using WHAM.

Elastic Model. To evaluate the results of the dynamical simulations and free energy calculations, we compare the simulation results to a simplified elastic model for invagination of a particle in a membrane. Our elastic model closely follows that of ref 15, but we consider an infinite tensionless membrane rather than a vesicle.

The total energy of the particle–membrane system arises from the energy of adhesion between the particle and the membrane (e_{ad}) and the elastic energy of the membrane (e_{m}). Following the simulation model, we assume that adhesion is mediated by short-range interactions with energy per area $-\epsilon^*$ so that the total energy of adhesion is $e_{\text{ad}} = -\epsilon^* a_{\text{wrap}}$ with a_{wrap} the area of the membrane in contact with the particle. Note that ϵ^* actually describes a free energy since it includes the effects of counterion dissociation and other entropic factors involved in particle associations, but following ref 15, we refer to it and the elastic terms described next as energies to emphasize that we are neglecting the (small) contribution to the free energy associated with fluctuations around the lowest free energy membrane configuration.

To calculate the elastic contributions to the energy, we consider the Helfrich Hamiltonian for an infinitesimally thin membrane³⁸

$$e_{\text{m}} = \int da \left(\sigma_s + \frac{\kappa}{2} (2H - C_0)^2 + \kappa_G K \right) \quad (9)$$

where σ_s is the surface tension, κ and κ_G are the bending rigidity and the Gaussian curvature modulus respectively, H and K are the mean and Gaussian curvatures, and C_0 is the spontaneous curvature. Our model membrane is symmetric and tensionless, so C_0 and σ_s are 0. We will use this elastic model to describe the budding process up until the point of scission at the neck, and thus the topology of the membrane remains constant. Assuming that the Gaussian curvature modulus κ_G is invariant throughout the membrane, the last term in eq (9) is constant under the Gauss-Bonnet theorem.³⁹ The elastic energy for a general configuration of the membrane is then given by

$$e_{\text{m}} = \int \frac{\kappa}{2} \left(\frac{1}{r_1} + \frac{1}{r_2} \right)^2 da \quad (10)$$

with r_1 and r_2 as the principal radii of curvature.

We follow Deserno et al.¹⁵ to assume that the following geometry closely corresponds to the lowest free energy configuration for a partially wrapped particle (Figure 4). There is an area a_{wrap} of the membrane tightly adhered to the particle with radius of curvature approximately equal to the particle radius R , and a rim area, a_{rim} , between the point at which the membrane separates from the particle and where it recovers a flat configuration. Because the particle is a featureless sphere, we assume that the lowest free energy configuration is axisymmetric, to give the energy

$$e = e_{\text{ad}} + e_{\text{wrap}} + e_{\text{rim}} \\ = -a_{\text{wrap}} \epsilon^* + \kappa \left[\frac{2a_{\text{wrap}}}{R^2} + \int \frac{da_{\text{rim}}}{2} \left(\frac{1}{r_1} + \frac{1}{r_2} \right)^2 \right] \quad (11)$$

where a_{rim} is the area of the rim surrounding the particle and r_1 and r_2 are the principal radii of curvature in the rim area.

We now recast eq (11) in terms of two new variables, the latitudinal degree of wrapping θ and the penetration p , which is the distance the particle travels along the direction normal to

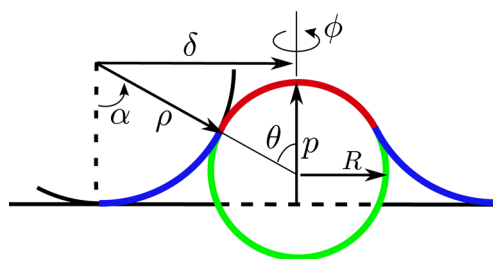


Figure 4. Cross-section of the 3D geometry used for the elastic model of a membrane wrapping a particle of radius R . The particle, depicted as a green sphere, adheres to a section of the membrane in red with area a_{wrap} . The surrounding membrane, with area a_{rim} , drawn in blue, decays toward the flat configuration. The shape of this surrounding membrane is taken to be a section of a torus for simplicity. δ and ρ stand for the outer and inner radii of the section of the torus formed by the rim region, and α and ϕ represent the polar and azimuthal angles of spherical coordinates. For a given penetration, p , there is a wrapping degree, θ , that minimizes the elastic energy.

the flat membrane, measured from the point at which the surface of the particle first touches the flat membrane. The maximum possible degree of wrapping for a given penetration is thus defined by $\theta_{\text{max}} = \arccos(1 - p/R)$. Note that while the theoretical penetration describes the vertical distance between the particle top and the position of the flat membrane, the computational definition describes the vertical distance between the particle top and the center of mass of the membrane. The two definitions are thus qualitatively the same but not identical.

In Figure 4, a schematic of the system is depicted as a 2-D cross-sectional cut, in which the red line represents the section of the membrane bound to the particle and the blue line represents the rim region. As shown in the schematic, we assume that the rim corresponds to a section of a torus (appearing as a circular arc in the 2-D cross-section). Although this is only one of the multiple shapes the rim can form, it was shown to closely correspond to solutions from a full variational calculation in ref.¹⁵ and allows us to write the geometric properties of the system as explicit functions of our parameters. In particular, the radius of the torus depends uniquely on the particle size R , the wrapping degree θ and the penetration p ; the area element on a torus and the two principal radii of curvature are¹⁵ $da_{\text{rim}} = \rho(\delta - \rho \sin \alpha) d\alpha d\phi$, $r_1 = \rho$, and $r_2 = -((\delta - \rho \sin \alpha)/(\sin \alpha))$, with α and ϕ as the polar and azimuthal angles in spherical coordinates. With the new parametrization, the area of the membrane in contact with the particle for a wrapping degree θ turns out to be $a_{\text{wrap}}(\theta) = 2\pi R^2(1 - \cos(\theta))$.

Therefore, the energy of the system can be written in the following way:

$$e = \left(-\frac{A\epsilon^*}{2} + 4\pi\kappa \right) (1 - \cos \theta) \\ + \pi\kappa \int_0^\theta \rho |\delta - \rho \sin \alpha| \left(\frac{1}{\rho} - \frac{\sin \alpha}{\delta - \rho \sin \alpha} \right)^2 d\alpha \quad (13)$$

$$\rho = \frac{p + R(\cos \theta - 1)}{2 \sin^2(\theta/2)} \quad (14)$$

$$\delta = -\frac{p}{\tan(\theta/2)} \quad (15)$$

where $\theta \in (0, \theta_{\max})$, $\theta_{\max} = \arccos(1 - p/R)$ and $A = 4\pi R^2$ is the surface area of the particle. For a given bending rigidity, particle size and membrane-particle interaction, the energy only depends on the penetration p and the wrapping degree θ .

RESULTS

Elastic Theory Phase Diagram. For each value of p we minimize the energy eq (13) with respect to θ to obtain the membrane configuration and corresponding energy as a function of penetration alone. The results of the minimization are shown in Figure 5. Here, the dashed line is the binodal,

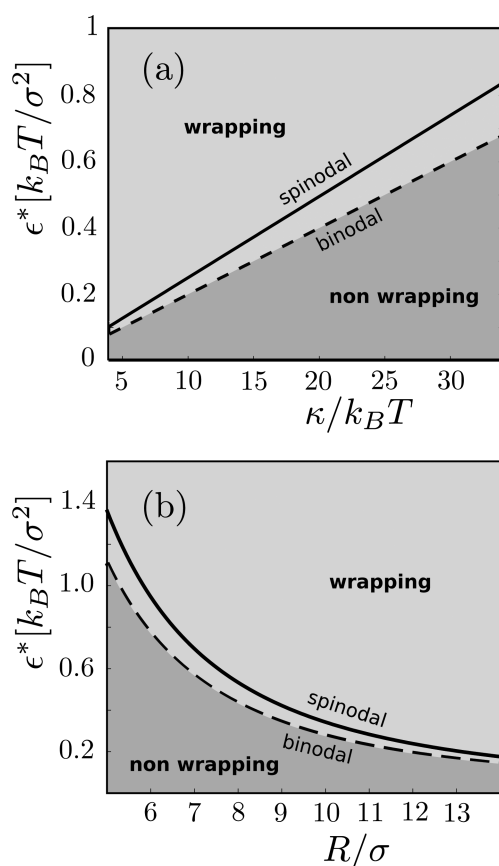


Figure 5. Phase diagrams obtained from the energy minimization in eq (13) (a) as a function of ϵ^* and κ for constant $R = 10\sigma$ and (b) as a function of the particle size, R , and the adhesion free energy per area, ϵ^* , for constant bending rigidity $\kappa = 13.9k_B T$. The binodal ($\epsilon^* = (2\kappa/R^2)$) above which wrapping is energetically favorable is indicated by a dashed line and the spinodal, above which wrapping proceeds without an energy barrier, is shown by a solid line.

given by $\epsilon^* = 2\kappa/R^2$, below which wrapping is energetically unfavorable, and the solid line denotes the spinodal, above which wrapping proceeds without any energetic barrier. In between the lines there is a barrier to wrapping which begins at $p = 0$, meaning that there are no long-lived partially wrapped states consistent with this theory for infinite membranes.

Simulation Results. To understand the influence of membrane and particle properties on budding, we began by performing dynamical simulations for a range of particle-membrane interaction strengths, ϵ , particle radius R , and ω_σ which controls the areal density of lipids, the bending rigidity κ , and diffusion rates within the membrane, as described in the Membrane Model section. Different values of these parameters

lead to dramatically different behaviors, as shown in the phase diagrams presented in Figure 6. First we note that the behaviors

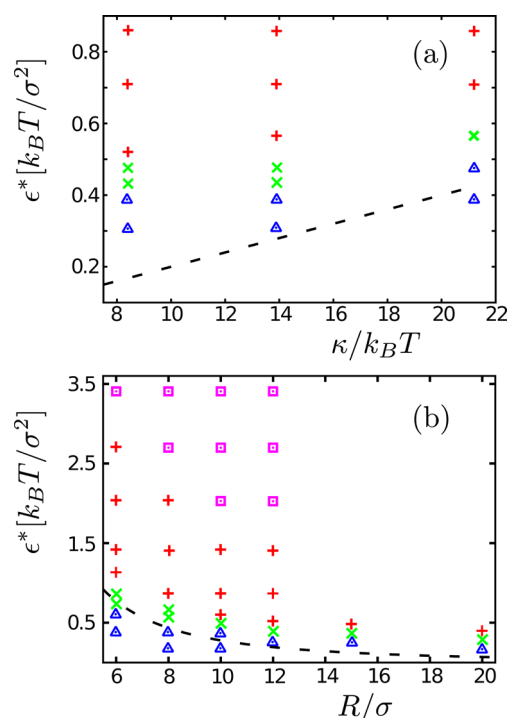


Figure 6. Phase diagrams obtained from MD simulations and free energy calculations (a) as a function of ϵ and κ for constant $R = 10\sigma$ and (b) as a function of the particle size R and adhesion free energy ϵ^* for constant bending rigidity, $\kappa = 13.9k_B T$. Parameter sets are identified as those which lead to no wrapping (Δ symbols), long-lived partially wrapped structures (\times symbols), complete wrapping ($+$ symbols), and those for which the membrane undergoes rupture prior to budding (\square symbols). The wrapping binodal predicted by the elastic theory is shown as a dashed line on each plot. The relationship between the adhesion free energy ϵ^* and the headgroup-particle attractive well depth ϵ is given in eq (7) and in Figure 3.

can be grouped into four classes, which we illustrate by describing trajectories observed for various values of ϵ and constant values of $\kappa = 13.9k_B T$ and $R = 12\sigma$ (Figure 7).

For weak adhesion strengths ϵ , no wrapping occurs; the membrane continues to exhibit only the usual spectrum of thermal fluctuations (Figure 8) after the particle adheres to it, and the penetration oscillates around negative values (Figure 7, case for $\epsilon = 0.5\epsilon_0$). For a narrow intermediate range of $0.6 < \epsilon/\epsilon_0 \lesssim 1.2$, the particle adheres to the membrane, but wrapping ceases at a partially wrapped state (Figure 9), after which the degree of particle penetration into the membrane fluctuates around a steady value (Figure 7, cases for $\epsilon = 1.0\epsilon_0$ and $\epsilon = 1.2\epsilon_0$). The average value of the penetration remained unchanged for as long as we simulated (up to $4 \times 10^4 \tau_0$). The final degree of penetration in this arrested state increases with ϵ , until approximately the point at which the particle is half wrapped (Figure 7, case for $\epsilon = 1.2\epsilon_0$).

A further increase in ϵ results in the next class of trajectories (Figure 7, case for $\epsilon = 2.0\epsilon_0$ and $3.0\epsilon_0$), in which the particle is completely encapsulated (Figure 10). In this case, wrapping proceeds steadily until the particle is completely surrounded by membrane except for a narrow neck region (Figure 10d). Wrapping is then completed when a thermal fluctuation causes the neck to break and have its sides fused (Figure 10e), after

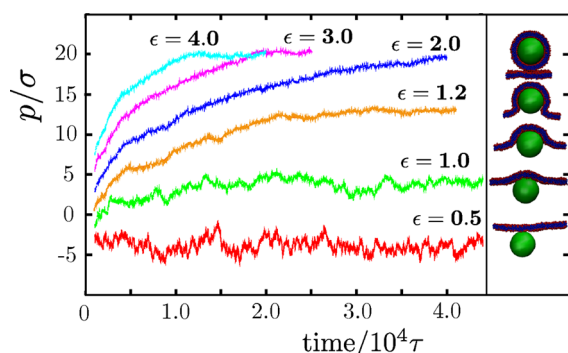


Figure 7. Particle penetration into the membrane, p , as a function of time for MD trajectories with different values of the adhesion energy ϵ for a system with particle radius $R = 12\sigma$ and membrane bending rigidity $\kappa = 13.9k_B T$. For $\epsilon = 0.5\epsilon_0$ (red line) no wrapping occurs. For $\epsilon = 1.0\epsilon_0$ (green line) and $1.2\epsilon_0$ (orange line), budding becomes stalled at a partially wrapped state whose value increases with ϵ . For $\epsilon = 2.0\epsilon_0$ (blue line), 3.0 (pink line), and 4.0 (cyan line) the particle undergoes complete encapsulation. On the right, slices of the system for corresponding values of p are shown. Images were generated using VMD.⁴¹

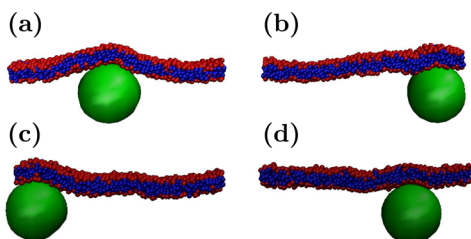


Figure 8. Adhesion without wrapping. Slices of configurations extracted from MD simulations with $\epsilon = \epsilon_0$, $R = 10\sigma$, and $\kappa = 13.9k_B T$. Times shown are (a) $t = 5 \times 10^3\tau_0$, (b) $4 \times 10^4\tau_0$, (c) $6 \times 10^4\tau_0$, and (d) $1 \times 10^5\tau_0$.

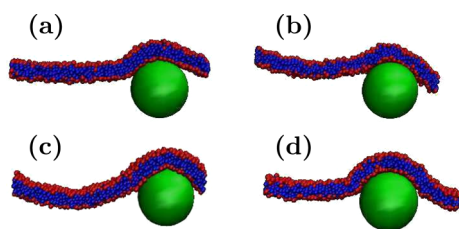


Figure 9. Long-lived partial wrapping. Slices of configurations extracted from MD simulations with $\epsilon = 1.3\epsilon_0$, $R = 10\sigma$, and $\kappa = 13.9k_B T$. The particle remains partially wrapped for the length of the simulation ($t = 4 \times 10^4\tau_0$). (a) $t = 5 \times 10^3\tau_0$, (b) $1.5 \times 10^4\tau_0$, (c) $2.5 \times 10^4\tau_0$, and (d) $3 \times 10^4\tau_0$.

which the fully wrapped particle diffuses away from the membrane (Figure 10f). Since fusion is a stochastic event, the budding time can be variable and we have observed neck configurations lasting between $500\tau_0$ and $5000\tau_0$. The elastic theory predicts that the shape and length of the neck depend on the balance between the adhesion energy and the bending energy, with strong adhesion favoring a short neck and large bending energies favoring a long neck. The simulation results are consistent with this prediction; example configurations are shown in Figure 11. The figure shows snapshots from simulations with particle radius $R = 6\sigma$, bending rigidity $\kappa = 13.9k_B T$ and different values of ϵ . A small particle size was chosen for the figure because the relationship between neck

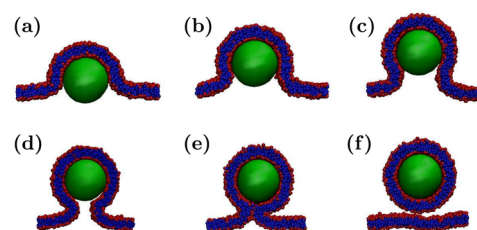


Figure 10. Wrapping. Slices of configurations at different times extracted from MD simulations with $\epsilon = 3\epsilon_0$, $R = 10\sigma$, and $\kappa = 13.9k_B T$. The membrane wraps the particle (a–d) until a neck or channel connecting the flat bilayer and the membrane surrounding the particle forms (e). Thermal fluctuations break this narrow neck, resulting in the encapsulated particle escaping from the membrane (f). Configurations are shown for times (a) $t = 5 \times 10^3\tau_0$, (b) $1 \times 10^4\tau_0$, (c) $1.5 \times 10^4\tau_0$, (d) $1.95 \times 10^4\tau_0$, (e) $2 \times 10^4\tau_0$, and (f) $2.5 \times 10^4\tau_0$.

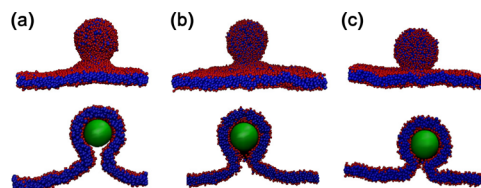


Figure 11. Neck profile depends on the adhesion strength. Membrane configurations are shown shortly before the completion of budding for $R = 6\sigma$, $\kappa = 13.9k_B T$ and different adhesion strengths. (a) A relatively small adhesion strength, $\epsilon = 3\epsilon_0$, leads to a long neck. (b) For $\epsilon = 4\epsilon_0$ the neck is shorter. (c) For $\epsilon = 5\epsilon_0$, close to the adhesion strength that leads to membrane rupture, the neck length is comparable to the height of typical membrane fluctuations. The top row of images shows a side view of system configurations and the bottom row of images gives the corresponding side-view slices.

configuration and adhesion energy is most easily visualized when high membrane curvature is required for wrapping.

The fact that fusion is accessible within the course of a typical simulation is an interesting contrast between the model studied here and that studied by Smith et al.,²² where fusion was observed only for inhomogeneous membranes, where the line tension arising from phase separated domains with an interface surrounding the particle was needed to promote fusion. The difference in fusion behavior between the two models could arise from the fact that Smith et al.²² consider lipid molecules with two tails, but other parameter differences (e.g., range of bending moduli considered or lipid cohesion) might also play a role.

For higher values of ϵ wrapping proceeds extremely rapidly (Figure 7, case for $\epsilon = 4.0\epsilon_0$) as there is a strong driving force to increase the number of head-particle interactions (Figure 12). As the curvature of the membrane in the vicinity of the wrapping front increases, the membrane structure undergoes ruptures in that region (Figure 12d), and a pore forms in the membrane (Figure 12e). The pore size increases with the adhesion energy, with a maximum diameter of the order of the particle radius. The fully encapsulated particle then diffuses away and the pore heals through thermal motions of the lipids. The formation of a pore during these budding trajectories resembles the process by which a hydrophobic nanoparticle passes through membranes in the simulations described in,^{23,40} but the physical driving forces are different in this case and the pore arises for kinetic reasons. Namely, the collective wrapping process proceeds more slowly than ruptures form in the

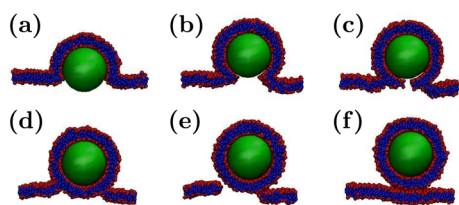


Figure 12. Wrapping via membrane rupture. Slices of configurations at different times extracted from MD simulations with $\varepsilon = 5\varepsilon_0$, $R = 10\sigma$, and $\kappa = 13.9k_B T$. Particle wrapping (a and b) leads to the formation of a pore (c and d). Eventually, the enveloped particle leaves the membrane (e) and the pore closes (f). Configurations shown occurred at times (a) $t = 2 \times 10^3 \tau_0$, (b) $5 \times 10^3 \tau_0$, (c) $5.4 \times 10^3 \tau_0$, (d) $5.6 \times 10^3 \tau_0$, (e) $8 \times 10^3 \tau_0$, and (f) $9.5 \times 10^3 \tau_0$.

membrane due to the large driving force to increase particle-headgroup contacts.

Free Energy Calculations and the Partially Wrapped State. We were particularly interested in the partially wrapped states seen in the dynamical simulations, as the elastic model predicts no stable or metastable partially wrapped states. To determine whether or not these observations corresponded to equilibrium configurations, the free energy was calculated as a function of the penetration using umbrella sampling (Simulations section). Calculated free energy projections are shown for three values of ε in Figure 13, for which the finite-time

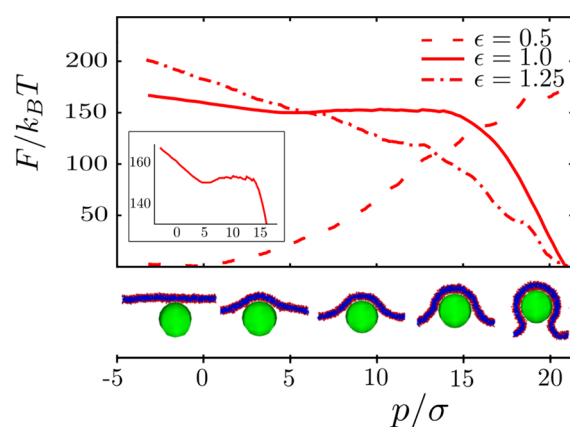


Figure 13. Free energy profiles as a function of the penetration, p , calculated from MD simulations using umbrella sampling are shown for $R = 12\sigma$, $\kappa = 13.9k_B T$, and indicated values of ε . In the inset, the local minimum for $\varepsilon = 1.0$ can be observed. At the bottom, slices of the system as a function of the penetration are shown.

dynamical simulations respectively ended in no wrapping ($\varepsilon = 0.5\varepsilon_0$), partial wrapping ($\varepsilon = \varepsilon_0$), and complete wrapping ($\varepsilon = 1.25\varepsilon_0$). For the cases of full wrapping and no wrapping, the calculated free energy projections are consistent with the dynamics results. Namely, for $\varepsilon = 0.5\varepsilon_0$ the minimum free energy value corresponds to no wrapping with a steep penalty for increasing penetration, while for $\varepsilon = 1.25\varepsilon_0$ the free energy decreases monotonically with increasing penetration until the particle is completely wrapped.

In contrast, the minimum value in the free energy profile for $\varepsilon = 1.0\varepsilon_0$ does not correspond to the partially wrapped state observed in the dynamical simulations, but rather corresponds to complete wrapping. The free energy profile does show a local minimum at $p \approx 5\sigma$, which corresponds to the penetration of the partial wrapping configuration, indicating that the states

observed in the dynamical trajectories are metastable. However, the well depth is only a few $k_B T$ while partially wrapped states continue for as long as we have simulated $4 \times 10^4 \tau_0$. We therefore performed further comparison of umbrella sampling results to dynamical trajectories. We chose a set of configurations from the umbrella sampling trajectories with different values of p . For each such configuration we performed several unbiased MD trajectories initialized with velocities using different random number seeds to obtain a crude estimate of the commitment probability.⁴² We found that trajectories initiated from configurations with small values of $p \lesssim 5\sigma$ fluctuate around that value and configurations with $p \gtrsim 18.8\sigma$ progressed steadily to complete wrapping. However, configurations with $5\sigma \leq p \lesssim 18.8\sigma$ tended to fluctuate around the value of p corresponding to their initial configuration, which is inconsistent with the free energy profile for $p \geq 15\sigma$ and raises the possibility of an additional slow degree of freedom at moderate ε . That is, while p is a suitable order parameter for determining the free energies of the stable states, it may not be a complete reaction coordinate capable of describing the dynamics along the transition.⁴²

It is not necessary to identify a perfect reaction coordinate to fulfill our primary objective of understanding the phase behavior, but we did examine other potentially relevant dynamical degrees of freedom. Analysis of umbrella sampling configurations during the equilibration phase of the calculation indicates that, when the particle is held at a fixed penetration, the membrane configuration gradually relaxes to a state of increased adhesion (Figure 14). Thus a reaction coordinate

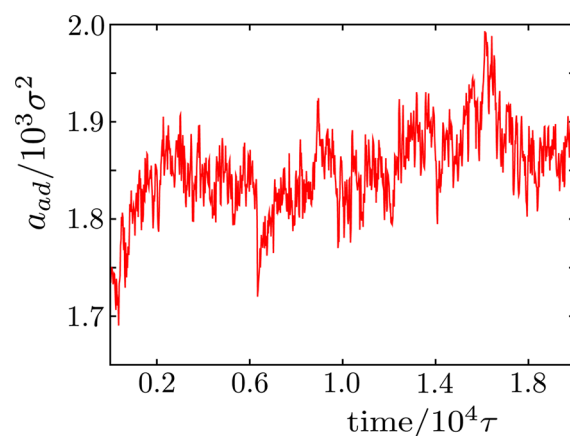


Figure 14. Evolution of the membrane area in contact with the particle as a function of time for MD simulations in which a smoothed Heaviside biasing potential eq (8) holds the penetration in the vicinity of $p = p_0 = 16.875\sigma$. The time courses are averaged over 20 independent trajectories.

capable of completely describing the transition dynamics may need to include an additional collective variable that describes adhesion and/or membrane bending. Investigating this possibility, however, is beyond the scope of the present work focused on the phase behavior.

Comparison between Computational and Theoretical Phase Diagrams. Based on the results of dynamical simulations over a wide range of parameters, as well as umbrella sampling at parameter sets near the transition between no wrapping and wrapping, we determined phase diagrams as functions of adhesion energy ε , membrane bending modulus κ , and particle radius R (Figure 6). To enable

comparison with the elastic theory (eq (11), Figure 5), it is essential to note the theoretical parameter ε^* corresponds to the adhesion free energy rather than simply the depth of the headgroup-particle attractive potential well ε (see the Methods section). Therefore, we plot the data as a function of the adhesion free energy per area ε^* ; the relationship between ε^* and ε is shown in Figure 3. The parameter sets for which nonwrapping is the equilibrium configuration are shown with Δ symbols, while the parameter sets which lead to equilibrium wrapping are separated into those which involve long-lived partially wrapped structures (\times symbols), complete wrapping ($+$ symbols), and those for which the membrane undergoes rupture prior to budding (\square symbols). The wrapping binodal predicted by the elastic theory is shown as a dashed line on each plot. We see that while the theory and simulations agree to within about $0.2k_B T$, the theoretical binodal is below the computational results. This discrepancy could occur because we have not accounted for the configurational entropy contributed by the lipids during adhesion or due to the fact that the theory assumes an infinitesimally thin membrane. A more significant difference between the computational results and the elastic theory is that, as noted above, the theory does not predict the existence of the metastable partially wrapped states.

DISCUSSION

Our dynamical simulations of a minimal molecular model for the process of passive endo- or exocytosis identified four classes of behaviors resulting from the interaction of a particle with a membrane: no wrapping or adhesion resulting in a minimal perturbation of membrane configurations, partial wrapping, complete wrapping, and wrapping via rupture of the membrane. Equilibrium calculations showed that there are only two equilibrium configurations, corresponding to no wrapping or complete wrapping, and this equilibrium phase behavior for the molecular model shows strong agreement with the predictions of a simplified elastic theory.¹⁵ The primary difference between the elastic model and the finite-time dynamical simulation results is the appearance of long-lived partial wrapping states.

Since the long-lived partially wrapped states seen in this study could be significant for dynamical, time-sensitive particle uptake processes such as endocytosis or viral budding in living organisms, it is worth comparing them to observations of other models. Most closely related to our results, Yue and Zhang²³ study a model comparable to ours except that the particle is coated with ligands that experience attractive interactions with membrane lipids. It appears that some of the configurations which they denote as “adhesion” correspond to our long-lived partially wrapped states; however, it would be necessary to perform free energy calculations to determine whether they are metastable as we find here. In contrast to their model, we do not identify any parameter sets for which the particle partially penetrates into the hydrophobic interior of the membrane. Partially wrapped states have also been predicted from equilibrium theories in the context of finite-sized systems. Deserno et al.¹⁵ examined the budding of a colloid from the interior of a spherical vesicle using the same Hamiltonian as introduced in elastic theory described above. They found that partial wrapping corresponds to the equilibrium state when the vesicle size is on the order of the colloid diameter due to the increase in curvature energy of the finite-sized vesicle. We similarly obtain partial wrapping configurations as equilibrium solutions if we introduce finite size into the elastic theory studied here, eq (11), by minimizing the energy of the elastic

theory, eq (13), with the total membrane surface area constrained to $16R^2$, so that the wrapping area plus the rim area cannot exceed the total area. Zhang and Nguyen¹⁷ also identify partially wrapped states as equilibrium solutions to an elastic theory, but they observed that the catenoid configuration is the only solution to the full variational problem for a tensionless infinite membrane. This solution implies that the elastic energy of the rim is always zero, and thus wrapping is only determined by the balance between the bending energy in the wrapped region and the adhesion energy, which does not lead to partial wrapping states. Because the toroid approximation for membrane configurations assumed in our elastic model is more restrictive than the full variational problem, the wrapping binodal shown in Figure 5 is shifted to slightly higher values of the adhesion energy ε than obtained for their theory,¹⁷ but the behavior is qualitatively unchanged. Importantly, neither theory predicts the partially wrapped state as a metastable configuration in an infinite membrane.

The membrane size in our simulations was chosen large enough to ensure that the theoretically predicted finite-size effects would not affect our results. To confirm that this was the case, we ran additional dynamical simulations and umbrella sampling calculations with membranes which were 50% and 100% larger (16 200 and 28 800 lipids respectively). The simulation results were the same for all three membrane sizes.

Finally, we consider our minimal model for passive endo- or exocytosis in the context of physical systems. Based on the length scales discussed in the Parameters section, the particle diameters in our simulations range from 9 to 36 nm. Nanoparticles are available in a wide range of sizes, with particles smaller than 50 nm undergoing the most efficient uptake,⁴³ although interactions between nanoparticles can reduce that radius when smaller nanoparticles cluster and bud together.¹⁸ Our simulated particles are somewhat smaller than the size of viral capsids that undergo budding, which range from about 40 nm (e.g., hepadnavirus⁴⁵) to hundreds of nanometers, but the results can be extrapolated into that range. As shown in Figure 5 the adhesion-wrapping transition decreases with radius as $1/R$ for constant bending rigidity.

The limit of a tensionless membrane studied here could become a poor approximation if adhesion to the budding particle leads to crystalline order, but we did not see evidence of that in our simulations even at the highest adhesion energies studied. Other cases in which a tensionless membrane limit might break down include multicomponent membranes with lipids of different chain lengths or phase-separated regions leading to line tensions and thus spontaneous curvature.⁴⁴ In those cases, the range of adhesion energies that allow budding would be shifted according to the gain or loss in bending energy from the spontaneous curvature.

Our simulation results indicate that the existence of attractive interactions between a particle and lipid head groups, which has been proposed as the minimal requirement for viral budding,^{26,32} is indeed sufficient to drive efficient wrapping. However, to avoid stalled partially wrapping states and membrane rupture, the system would be confined to a relatively narrow range of adhesion strengths spanning about $2k_B T/\sigma^2$ (the $+$ symbols in Figure 6). While this result is qualitative, since the range increases in width with the particle size and the three-bead representation of the lipid molecule may lead to model membranes which are more susceptible to rupture than those comprised of a more realistic lipid, it does establish important constraints on viral evolution if budding is

limited to these ingredients. However, depending on the viral system, a number of additional phenomena contribute to budding, including membrane-associated viral envelope or spike proteins, preferential budding from lipid rafts,⁴⁶ the use of cytoskeletal machinery to actively drive or assist budding^{6,47} or scission,^{7,27} and the ability of the virus to remodel cell membrane properties.²⁸ These effects can broaden the range of functional adhesion energies; for example, using actin to drive assembly and budding⁶ could enable efficient viral egress even for adhesion energies at which spontaneous dynamics become stalled. In this case the presence of a barrier to budding could serve as a regulatory feature. The agreement between our simulation results and the elastic theory over some ranges of parameter space indicates that some or all of these effects could in principle be captured by extending existing elastic theories along the lines of Liu et al.'s description of active endocytosis,⁴ but care would be required to include all relevant slow degrees of freedom near transitions between wrapping and no wrapping.

AUTHOR INFORMATION

Corresponding Author

*E-mail: teresa.ruiz@uam.es; hagan@brandeis.edu.

Notes

The authors declare no competing financial interest.

ACKNOWLEDGMENTS

This work was supported by Award Number R01AI080791 from the National Institute Of Allergy And Infectious Diseases, MODELICO Grant (S2009/ESP-1691) from Comunidad Autónoma de Madrid and FIS2010-22047-C05-01 Grant from Ministerio de Ciencia e Innovación de España. Computational resources were provided by the National Science Foundation through TeraGrid computing resources (LONI QueenBee, Purdue Condor, and SDSC Trestles) and the Brandeis HPCC.

REFERENCES

- Nel, A. E.; Mädler, L.; Velegol, D.; Xia, T.; Hoek, E. M. V.; Somasundaran, P.; Klaessig, F.; Castranova, V.; Thompson, M. *Nat. Mater.* **2009**, *8*, 543–557.
- Mitragotri, S.; Lahann, J. *Nat. Mater.* **2009**, *8*, 15–23.
- Poland, C. A.; Duffin, R.; Kinloch, I.; Maynard, A.; Wallace, W. A. H.; Seaton, A.; Stone, V.; Brown, S.; Macnee, W.; Donaldson, K. *Nat. Nanotechnol.* **2008**, *3*, 423–428.
- Liu, J.; Sun, Y.; Drubin, D. G.; Oster, G. F. *PLoS Biol.* **2009**, *7*, e1000204.
- Welsch, S.; Müller, B.; Kräusslich, H.-G. *FEBS Lett.* **2007**, *581*, 2089–2097.
- Gladnikoff, M.; Shimon, E.; Gov, N. S.; Rouso, I. *Biophys. J.* **2009**, *97*, 2419–2428.
- Baumgartel, V.; Ivanchenko, S.; Dupont, A.; Sergeev, M.; Wiseman, P. W.; Krausslich, H.-G.; Brauchle, C.; Müller, B.; Lamb, D. C. *Nat. Cell Biol.* **2011**, *13*, 469–474.
- Helenius, A.; Fries, E.; Kartenbeck, J. *J. Cell Biol.* **1977**, *75*, 866–880.
- von Bonsdorff, C. H.; Harrison, S. C. *J. Virol.* **1978**, *28*, 578–583.
- Bihan, O. L.; Bonnafous, P.; Marak, L.; Bickel, T.; Trépout, S.; Mornet, S.; Haas, F. D.; Talbot, H.; Taveau, J.-C.; Lambert, O. *J. Struct. Biol.* **2009**, *168*, 419–425.
- Hurley, J. H.; Boura, E.; Carlson, L.-A.; Rózycki, B. *Cell* **2010**, *143*, 875–887.
- Solon, J.; Gareil, O.; Bassereau, P.; Gaudin, Y. *J. Gen. Virol.* **2005**, *86*, 3357–3363.
- Popova, E.; Popov, S.; Göttlinger, H. G. *J. Virol.* **2010**, *84*, 6590–6597.
- Rossman, J. S.; Jing, X.; Leser, G. P.; Lamb, R. A. *Cell* **2010**, *142*, 902–913.
- Deserno, M.; Gelbart, W. M. *J. Phys. Chem. B* **2002**, *106*, 5543–5552.
- Gao, H. J.; Shi, W. D.; Freund, L. B. *Proc. Natl. Acad. Sci. U.S.A.* **2005**, *102*, 9469–9474.
- Zhang, R.; Nguyen, T. T. *Phys. Rev. E* **2008**, *78*, 051903.
- Chaudhuri, A.; Battaglia, G.; Golestanian, R. *Phys. Biol.* **2011**, *8*, 046002.
- Fošnarić, M.; Iglić, A.; Kroll, D. M.; May, S. J. *Chem. Phys.* **2009**, *131*, 105103.
- Li, Y.; Gu, N. J. *J. Phys. Chem. B* **2010**, *114*, 2749–2754.
- Ginzburg, V. V.; Balijepalli, S. *Nano Lett.* **2007**, *7*, 3716–3722.
- Smith, K. A.; Jasnow, D.; Balazs, A. C. *J. Chem. Phys.* **2007**, *127*, 084703.
- Yue, T. T.; Zhang, X. R. *Soft Matter* **2011**, *7*, 9104–9112.
- Yang, K.; Ma, Y. Q. *Aust. J. Chem.* **2011**, *64*, 894–899.
- Vacha, R.; Martinez-Veracoechea, F. J.; Frenkel, D. *Nano Lett.* **2011**, *11*, 5391–5395.
- Garoff, H.; Hewson, R.; Opstelten, D. J. *Microbiol. Mol. Biol. Rev.* **1998**, *62*, 1171–1190.
- Demirov, D. G.; Freed, E. O. *Virus Res.* **2004**, *106*, 87–102.
- Chan, R. B.; Tanner, L.; Wenk, M. R. *Chem. Phys. Lipids* **2010**, *163*, 449–459.
- Cooke, I. R.; Kremer, K.; Deserno, M. *Phys. Rev. E* **2005**, *72*, 011506.
- Weeks, J. D.; Chandler, D.; Andersen, H. C. *J. Chem. Phys.* **1971**, *54*, 5237–+.
- Grest, G. S.; Kremer, K. *Phys. Rev. A* **1986**, *33*, 3628–3631.
- Garoff, H.; Sjöberg, M.; Cheng, R. H. *Virus Res.* **2004**, *106*, 103–116.
- Frenkel, D.; Smit, B. *Understanding molecular simulation: from algorithms to applications*, 2nd ed.; Academic: San Diego, CA, 2002.
- Kolb, A.; Dünweg, B. *J. Chem. Phys.* **1999**, *111*, 4453–4459.
- Torrie, G. M.; Valleau, J. P. *J. Comput. Phys.* **1977**, *23*, 187–199.
- Kumar, S.; Bouzida, D.; Swendsen, R. H.; Kollman, P. A.; Rosenberg, J. M. *J. Comput. Chem.* **1992**, *13*, 1011–1021.
- Grossfield, A. WHAM: the weighted histogram analysis method, version 2.0.6. <http://membrane.urmc.rochester.edu/content/wham>.
- Helfrich, W. Z. *Naturforsch. C* **1973**, *C 28*, 693–703.
- do Carmo, M. P. *Differential Geometry of Curves and Surfaces*; Prentice Hall: Upper Saddle River, NJ, 1976.
- Li, Y.; Chen, X.; Gu, N. J. *J. Phys. Chem. B* **2008**, *112*, 16647–16653.
- Humphrey, W.; Dalke, A.; Schulten, K. *J. Mol. Graph.* **1996**, *14*, 33–38.
- Dellago, C.; Bolhuis, P. G.; Geissler, P. L. *Adv. Chem. Phys.* **2002**, *123*, 1–78.
- Jiang, W.; Kim, B. Y. S.; Rutka, J. T.; Chan, W. C. W. *Nat. Nanotechnol.* **2008**, *3*, 145–150.
- Honnerkamp-Smith, A. R.; Cicuta, P.; Collins, M. D.; Veatch, S. L.; den Nijs, M.; Schick, M.; Keller, S. L. *Biophys. J.* **2008**, *95*, 236–246.
- Seeger, C.; Mason, W. S. *Microbiol. Mol. Biol. Rev.* **2000**, *64*, 51–68.
- Ono, A.; Freed, E. O. *Proc. Natl. Acad. Sci. U.S.A.* **2001**, *98*, 13925–13930.
- Taylor, M. P.; Koyuncu, O. O.; Enquist, L. W. *Nat. Rev. Microbiol.* **2011**, *9*, 427–439.